

Alma Mater Studiorum Università di Bologna
Archivio istituzionale della ricerca

Nonlinear conjugate gradient method for spectral tomosynthesis

This is the final peer-reviewed author's accepted manuscript (postprint) of the following publication:

Published Version:

Landi, G., Piccolomini, E.L., Nagy, J. (2019). Nonlinear conjugate gradient method for spectral tomosynthesis. INVERSE PROBLEMS, 35(9), 1-16 [10.1088/1361-6420/ab1c94].

Availability:

This version is available at: <https://hdl.handle.net/11585/698073> since: 2021-04-06

Published:

DOI: <http://doi.org/10.1088/1361-6420/ab1c94>

Terms of use:

Some rights reserved. The terms and conditions for the reuse of this version of the manuscript are specified in the publishing policy. For all terms of use and more information see the publisher's website.

This item was downloaded from IRIS Università di Bologna (<https://cris.unibo.it/>).
When citing, please refer to the published version.

(Article begins on next page)

This is the final peer-reviewed accepted manuscript of:

Nonlinear conjugate gradient method for spectral tomosynthesis

G Landi et al 2019 Inverse Problems 35 094003

The final published version is available online at: <http://dx.doi.org/10.1088/1361-6420/ab1c94>

Rights / License:

The terms and conditions for the reuse of this version of the manuscript are specified in the publishing policy. For all terms of use and more information see the publisher's website.

This item was downloaded from IRIS Università di Bologna (<https://cris.unibo.it/>)

When citing, please refer to the published version.

Nonlinear Conjugate Gradient Method for Spectral Tomosynthesis

G. Landi ¹, E. Loli Piccolomini ², J. Nagy ³

¹ Department of Mathematics, University of Bologna

² Computer Science and Engineering Department, University of Bologna

³ Department of Mathematics, Emory University

Abstract. Image reconstruction in spectral digital breast tomosynthesis requires solving a large-scale nonlinear inverse problem. Most numerical approaches on real data used a simplified linear (and hence incorrect) mathematical model to reduce the computational costs. The aim of this paper is to consider the use of a nonlinear conjugate gradient method for very large-scale nonlinear least squares problems, and apply it to spectral digital breast tomosynthesis. Numerical experiments on 3-dimensional phantom images illustrate the effectiveness and efficiency of the proposed scheme.

1. Introduction

Modern imaging technologies can very quickly acquire huge amounts of data. Not exhaustive examples of such technologies in the medical area are dynamic Magnetic Resonance [1], Magnetic Resonance fingerprinting [2], multienergy 3D x-ray Computed Tomography (CT) [3], echocardiography [4], and in industrial applications 3D ultrasound and x-ray CT.

In most of these applications a necessary step in the acquisition process is image reconstruction, which requires solving a large-scale nonlinear inverse problem of the form:

$$\mathbf{b} = K(\mathbf{x}) + \boldsymbol{\eta} \quad (1)$$

where $\mathbf{b} \in \mathbb{R}^M$ is a vector containing all acquired data, $\mathbf{x} \in \mathbb{R}^N$ is the image to be recovered, $K : \mathbb{R}^N \rightarrow \mathbb{R}^M$ is a function representing the action of the acquisition instrument on the object (and is therefore dependent on the particular application), and $\boldsymbol{\eta}$ is used to represent noise and other errors in the measured data. Since the problem is ill-posed, regularization is needed to compute a reliable solution. Supposing a normal distribution of the noise, a widely used approach is the variational formulation, where a large-scale nonlinear minimization problem of the form

$$\min_{\mathbf{x}} \quad \mathcal{F}(\mathbf{x}) = \frac{1}{2} \|\mathbf{r}(\mathbf{x})\|_2^2 + \gamma \omega(\mathbf{x}) \quad (2)$$

must be solved, where $\mathbf{r}(\mathbf{x}) = K(\mathbf{x}) - \mathbf{b}$ is the residual. The quality of the reconstruction depends on the choice of the regularization function $\omega(\mathbf{x})$; usually $\omega(\mathbf{x})$ is based on the L_2 or L_1 norm or it is equal to the null function. In the latter case, regularization is achieved by terminating the iteration at an appropriate point.

Many of the existing numerical methods for the solution of (2) are not usable in practice (i.e., in clinical settings) due to the large amount of data that needs to be processed (consider that N and/or M can be on the order of millions or billions), even in the case when we assume K is a linear function of x .

As a case study application, we consider in this paper the reconstruction of spectral Digital Breast Tomosynthesis (DBT) images. The problem is modelled by a nonlinear integral equation, whose discretization leads to a large-scale nonlinear minimization problem of the form (2). Such an optimization problem is challenging and a prototype implementation comparing different methods on reliable phantoms is an important contribution to the scientific research and a necessary step for the investment of the industrial research on this topic. However, in literature, there are few proposals for DBT spectral images reconstruction. In [5,6], the case $\omega(\mathbf{x}) = 0$ is considered and regularization is achieved by using heuristics to determine an appropriate stopping iteration. We remark that effective approaches to efficiently stop iterative methods for nonlinear ill-posed inverse problems remains an open problem with no satisfactory solution; the discrepancy principle can be applied, but it requires that the norm of the noise is known and it often produces oversmoothed solutions, while the other existing stopping criteria (such as L-curve and generalized cross validation GCV [7–10]) require extra computational work that is unfeasible in large-scale nonlinear problems. In [5], the Limited Memory BFGS (LBFGS) method is presented; in [6, 11], a variant of problem (2) is considered which is obtained by supposing the noise follows a Poisson distribution and by replacing the nonlinear least squares term with the Kullback-Leibler divergence. The corresponding optimization problem is solved by a gradient descent method. Finally, in [11], Poisson noise is suppose on the data and $\omega(\mathbf{x})$ has been chosen as the Total Variation (TV) regularization function; the resulting minimization problem is solved by an accelerated gradient method.

The aim of this paper is to give a contribution in computing an efficient solution of problem (2) for very large-scale problems, and for general nonlinear residuals $\mathbf{r}(\mathbf{x})$, as in DBT spectral imaging. When solving the DBT imaging problem, we have to take into account that it is extremely large-scale and that clinical trials need short computational times for the image reconstruction. For these reasons, we are interested in methods that compute only first derivatives and have low storage requirements. In this work we consider nonlinear conjugate gradient-type methods since they fulfill these computational and storage requirements and they convergence generally faster than gradient-type methods. Moreover, they do not have to address the ill-conditioning of the Hessian matrix as in the case of the LBFGS method. An excellent survey of conjugate gradient methods is given by Hager and Zhang [12]. We consider, for the numerical solution of the DBT imaging problem, a nonlinear conjugate gradient (NLCG) method

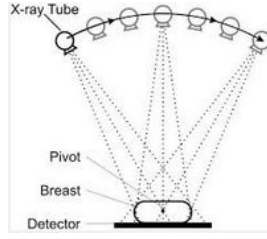


Figure 1. Geometry of a DBT system.

proposed Touati-Ahmed and Storey [13] and we compare its performance with that of two other first order methods: the accelerated gradient descent and a LMBFGS method. The results on a digital 3D phantom reproducing a real accreditation DBT phantom show that the NLCG method outperforms the other ones both in terms of precision and computational efficiency when used as an iterative regularization method (i.e, when $\omega(\mathbf{x}) = 0$) or as a solver for the TV-based optimization problem of the form (11) obtained when $\omega(\mathbf{x})$ is a smooth version of the TV function.

The paper can be outlined as follows. In Section 2, we present the spectral DBT application; in section 3, we describe the used NLCG method; in section 4, we show the numerical results obtained on a 3D digital phantom and finally, in section , we report some conclusions.

2. Case study: Spectral DBT image reconstruction

Digital Breast Tomosynthesis (DBT) [14–16] is a 3D Computed Tomography technique for the diagnosis of breast tumors. It is characterized by a limited angle geometry as represented in Figure 2. DBT is receiving growing interest in the medical community and it has been approved in the USA for screening. The reduced number of angles and the use of *soft x-rays* with a very low electron voltage produce a limited total radiation, which is almost equivalent to that of a traditional two view digital mammography. On the other hand, because DBT reconstructs a pseudo 3D image, it reduces the impact of overlapping tissues, and improves the detectability of even small structures of the breast.

DBT image reconstruction is usually performed by considering a monoenergetic approximation of the x-rays; in this case when a variational approach of the form (1) is used, $\mathbf{r}(\mathbf{x}) = K\mathbf{x} - \mathbf{b}$ is a linear function of \mathbf{x} and, since few data are available ($M \ll N$), the linear minimization problem is under-determined (see for example [17–19]). In addition, the monochromatic approximation leads to the so called beam-hardening artifacts [20].

By taking into account the polyenergetic nature of the x-rays, it is possible both to reduce the beam-hardening artifacts and to get quantitative information about the materials composing the objects, obtaining spectral images for each material. The disadvantage of this approach is that the problem arising from the discretization of

(1) is nonlinear and very difficult to solve. Some papers have been published in the last decades on algorithms for polyenergetic CT image reconstruction [3, 21, 22] and with multimaterial modeling [23, 24]. In [5, 6, 11] the authors propose a model for DBT polyenergetic spectral imaging, which we describe in the following in its essential steps; for more details, please refer to the cited papers.

The model is derived from the Beer's law [25] relating the object attenuation with the measured projections. We assume that the object being imaged is made up of a small number N_m of known materials; for example, in the case of breast imaging, these materials might include adipose and glandular tissue, possibly calcium, and iodine (which, when injected into the blood stream can highlight blood vessels and tissues). The 3D volume is discretized into N_v voxels, the detector is assumed to have N_p pixels, and the source emits x-rays from N_θ angles along an arc trajectory (see Figure 2). We suppose the x-ray beams are composed of N_e energy levels, and that the linear attenuation coefficients $\mu_{j,e}$ for each voxel j at the energy level e is approximated as a linear combination of individual materials with *unknown* weights $w_{j,m}$; that is,

$$\mu_{j,e} = \sum_{m=1}^{N_m} w_{j,m} c_{m,e} \quad (3)$$

where $c_{m,e}$ is the linear attenuation coefficient of the m -th material at e -th energy. We use $a_{i,j}^\theta$ to denote the length of the x-ray beam through the voxel j , incident onto the pixel i in the detector, with source at angle θ , and b_i^θ to denote the measured projection value in the i -th pixel, with source at angle θ . Finally, we indicate by s_e the energy fluence, which is a product of the x-ray energy with the number of incident photons at that energy.

Using this notation, and following [6], we have the following discrete image formation model

$$b_i^\theta = \sum_{e=1}^{N_e} s_e \exp \left(- \sum_{j=1}^{N_v} a_{i,j}^\theta \sum_{m=1}^{N_m} w_{j,m} c_{m,e} \right) + \eta_i^\theta, \quad \begin{cases} i = 1, \dots, N_p, \\ \theta = 1, \dots, N_\theta, \end{cases} \quad (4)$$

where η_i^θ represents noise measured at the detector at pixel i and angle θ , which can include x-ray scatter and electronic noise, and may be assumed to have a mixed Gaussian and Poisson distribution. We also assume that the weight fractions for each voxel add to 1, i.e:

$$\sum_{m=1}^{N_m} w_{j,m} = 1, \quad j = 1, \dots, N_v. \quad (5)$$

The equations given in (4) can be rewritten in matrix-vector form as

$$\mathbf{b} = \exp(-\mathbf{A}\mathbf{W}\mathbf{C}^T)\mathbf{s} + \boldsymbol{\eta} \quad (6)$$

where \mathbf{C} is an $N_e \times N_m$ matrix with entries $c_{e,m}$, \mathbf{W} is an $N_v \times N_m$ matrix with entries $w_{j,m}$, and \mathbf{s} is a vector with entries s_e . The matrix \mathbf{A} and the vectors \mathbf{b} and $\boldsymbol{\eta}$ are defined

in terms of blocks that depend on the angle θ . Specifically, if we define the $N_p \times N_v$ matrices $\mathbf{A}^{(\theta)}$ with entries $a_{i,j}^\theta$ and the N_p vectors $\mathbf{b}^{(\theta)}$ and $\boldsymbol{\eta}^{(\theta)}$ with, respectively, entries b_i^θ and η_i^θ , then

$$\mathbf{A} = \begin{bmatrix} \mathbf{A}^{(1)} \\ \mathbf{A}^{(2)} \\ \vdots \\ \mathbf{A}^{(N_\theta)} \end{bmatrix}, \quad \mathbf{b} = \begin{bmatrix} \mathbf{b}^{(1)} \\ \mathbf{b}^{(2)} \\ \vdots \\ \mathbf{b}^{(N_\theta)} \end{bmatrix}, \quad \boldsymbol{\eta} = \begin{bmatrix} \boldsymbol{\eta}^{(1)} \\ \boldsymbol{\eta}^{(2)} \\ \vdots \\ \boldsymbol{\eta}^{(N_\theta)} \end{bmatrix}.$$

We impose the constraint (5) through a variable substitution for

$$w_{j,1} = 1 - \sum_{m=2}^{N_m} w_{j,m}, \quad (7)$$

Then we define unknown \mathbf{X} as:

$$\mathbf{X} = [\mathbf{w}_2 \mid \mathbf{w}_3 \mid \dots \mid \mathbf{w}_{N_m}]. \quad (8)$$

where \mathbf{w}_i is the i -th column of \mathbf{W} , and define the $N_e \times (N_m - 1)$ matrix $\hat{\mathbf{C}}$ as

$$\hat{\mathbf{C}} = [\mathbf{c}_2 - \mathbf{c}_1 \mid \mathbf{c}_3 - \mathbf{c}_1 \mid \dots \mid \mathbf{c}_{N_m} - \mathbf{c}_1] \quad (9)$$

where \mathbf{c}_ℓ denotes the ℓ -th column of \mathbf{C} . With this notation, we have to solve the inverse problem (1) where

$$K(\mathbf{X}) = \exp \left(-\mathbf{A} \left(\mathbf{1}\mathbf{c}_1^T + \mathbf{X}\hat{\mathbf{C}}^T \right) \right). \quad (10)$$

Thus, the residual vector is

$$\mathbf{r}(\mathbf{X}) = K(\mathbf{X}) - \mathbf{b}.$$

and the optimization problem to be solved becomes

$$\min_{\mathbf{X}} \quad \mathbf{F}(\mathbf{X}) = \frac{1}{2} \|\mathbf{r}(\mathbf{X})\|_2^2 + \gamma \omega(\mathbf{X}) \quad (11)$$

We remark that typically the noise vector $\boldsymbol{\eta}$ is not available, but both \mathbf{s} and \mathbf{C} are known since an accurate estimate of the x-ray energy distribution can be obtained by using well-known spectra models and the linear attenuation coefficients $c_{e,m}$ can be derived by taking x-ray transmission measurements of objects with known dimension, density and material composition. Moreover, although we can use modestly sized problems for numerical simulations, in actual clinical applications typical values are $N_v = n_x \times n_y \times n_z$ with $n_x \simeq 1500$, $n_y \simeq 2000$ and $n_z \leq 100$, $N_p = n_x \times n_y$, $N_e \leq 30$ and $N_m \leq 4$.

In this paper, we also employ TV regularization, which can be very effective in detecting contours of homogeneous objects, such as masses. The TV regularization functional has the form

$$\omega(\mathbf{X}) = \mathbf{TV}_\beta(\mathbf{X}), \quad \mathbf{TV}_\beta(\mathbf{X}) := \sum_{\mathbf{i}=1}^{\mathbf{N}_m-1} \mathbf{TV}_\beta(\mathbf{x}_\mathbf{i})$$

where \mathbf{x}_i is the i -th column of \mathbf{X} (i.e, $\mathbf{x}_i = \mathbf{w}_{i+1}$), and $TV_\beta(\mathbf{X}_i)$ is a smoothed differentiable version of the TV of \mathbf{x}_i defined as [10]:

$$TV_\beta(\mathbf{x}_i) = \sum_{j=1}^{N_v} (\|\nabla \mathbf{x}_i^j\|_2^2 + \beta^2)^{1/2}$$

with β a positive small parameter. (Here, the letter superscripts indicate the individual component of vectors.) Hence, the smoothed TV of \mathbf{X} can be computed as

$$TV_\beta(\mathbf{X}) = \sum_{i=1}^{N_m-1} \sum_{j=1}^{N_v} (\|\nabla \mathbf{x}_i^j\|_2^2 + \beta^2)^{1/2}$$

where

$$\|\nabla \mathbf{x}_i^j\|_2^2 = (x_i^{j_x+1, j_y, j_z} - x_i^{j_x, j_y, j_z})^2 + (x_i^{j_x, j_y+1, j_z} - x_i^{j_x, j_y, j_z})^2 + (x_i^{j_x, j_y, j_z+1} - x_i^{j_x, j_y, j_z})^2$$

when forward differences are employed to approximate the gradient.

Let $\mathbf{J}(\mathbf{X})$ be the Jacobian of $\mathbf{r}(\mathbf{X})$; we emphasize that the n -th partial derivative of the data fitting term $\frac{1}{2}\|\mathbf{r}(\mathbf{X})\|^2$ of (11) can be computed as the scalar product of the n -th column of $\mathbf{J}(\mathbf{X})$ by the residual vector $\mathbf{r}(\mathbf{X})$ without storing the Jacobian matrix $\mathbf{J}(\mathbf{X})$ [5].

3. The Non Linear Conjugate Gradient method

Gradient-type, limited memory Quasi-Newton and nonlinear conjugate gradient methods are all described by the general iteration

$$\mathbf{X}^{(k+1)} = \mathbf{X}^{(k)} + \lambda_k \mathbf{p}^{(k)} \quad (12)$$

where $\mathbf{p}^{(k)}$ is a descent direction and λ_k is a step-length parameter computed by monotone line-search.

Gradient type methods are appealing since they do not need to evaluate the second derivative or to solve a linear system; moreover, they have low storage requirements since they need to store only the gradient vector in order to compute the search direction. However, they may be very slow. Acceleration techniques use a scaled direction

$$\frac{1}{\alpha_k} \mathbf{p}^{(k)} = -\nabla \mathbf{F}(\mathbf{X}^{(k)})$$

where Barzilai and Borwein-like rules are employed for the selection of the steplength α_k [26–28].

On the other hand, limited memory Quasi-Newton methods need a few vectors, say $\ell > 1$, to be stored but usually exhibit better convergence rate than gradient type methods. In [29], a specialized version of the LBFGS method is proposed for DBT imaging which uses Lavrentyev method for the search direction computation in order

to face the ill-conditioning of the LBFGS Hessian approximation. Such a specialized LBFGS method is defined by equation (12) where the search direction $\mathbf{p}^{(k)}$ solves the linear system

$$(\mathbf{B}^{(k)} + \mu_k \mathbf{I}) \mathbf{p}^{(k)} = -\nabla \mathbf{F}(\mathbf{X}^{(k)}) \quad (13)$$

where μ_k is a regularization parameter to be determined. The linear system (13) can be efficiently solved by an efficient recursive algorithm based on the Sherman-Morrison-Woodbury formula [30].

In a classic NLCG method, the descent direction is computed as

$$\mathbf{p}^{(k+1)} = -\nabla \mathbf{F}(\mathbf{X}^{(k)}) + \beta_k \mathbf{p}^{(k)}, \quad \mathbf{p}^{(0)} = -\nabla \mathbf{F}(\mathbf{X}^{(0)})$$

where β_k is the conjugate gradient parameter. Various formulas for β_k exist resulting in different conjugate gradient methods whose properties can be significantly different. Two well-known formulas for the β_k are the FletcherReeves (FR) [31] and PolakRibière (PR) [32] ones which respectively are

$$\beta_k^{\text{FR}} = \frac{\|\nabla \mathbf{F}(\mathbf{X}^{(k+1)})\|^2}{\|\nabla \mathbf{F}(\mathbf{X}^{(k)})\|^2} \quad (14)$$

and

$$\beta_k^{\text{PR}} = \frac{\nabla \mathbf{F}(\mathbf{X}^{(k+1)})^T \mathbf{Y}^{(k)}}{\|\nabla \mathbf{F}(\mathbf{X}^{(k)})\|^2} \quad (15)$$

where $\mathbf{Y}^{(k)} = \nabla \mathbf{F}(\mathbf{X}^{(k+1)}) - \nabla \mathbf{F}(\mathbf{X}^{(k)})$. These formulas are identical for a strongly convex quadratic function and the exact line search is performed, but they behave differently for general nonlinear functions and the inexact line search. Roughly speaking, FR method is characterized by strong convergence under appropriate assumptions and bad practical performance. By the other hand, PR method has good practical behavior and it may not converge in general. Both these methods have low storage requirements since they only need to store three vectors. In this work, we consider the hybrid method proposed by Touati-Ahmed and Storey in [13] which combines the FR and PR formulas in order to improve the behavior of the FR method while retaining its good convergence properties. The Touati-Ahmed and Storey (TAS) formula for the β_k parameter is

$$\beta_k = \max \{0, \min \{\beta_k^{\text{FR}}, \beta_k^{\text{PR}}\}\} \quad (16)$$

With this modification of the parameter β_k , the hybrid NLCG method of Touati-Ahmed and Storey possess the nice global convergence properties of the FR method and the desirable numerical performances of the PR method. In this work, we consider a non linear conjugate gradient method based on the TAS formula for the conjugate gradient parameter β_k and on the inexact Armijo's line search for the step length parameter λ_k . The general scheme of the considered NLCG method can be outlined as follows.

Algorithm: Non Linear Conjugate Gradient Method.

Initialization: Given $\mathbf{X}^{(0)}$, set $\mathbf{p}^{(0)} = -\nabla \mathbf{F}(\mathbf{X}^{(0)})$.

repeat

- (i) compute λ_k by using backtracking line search with Armijo's condition;
- (ii) set $\mathbf{X}^{(k+1)} = \mathbf{X}^{(k)} + \lambda_k \mathbf{p}^{(k)}$;
- (iii) compute

$$\beta_k^{\text{FR}} = \frac{\|\nabla \mathbf{F}(\mathbf{X}^{(k+1)})\|^2}{\|\nabla \mathbf{F}(\mathbf{X}^{(k)})\|^2}, \quad \beta_k^{\text{PR}} = \frac{\nabla \mathbf{F}(\mathbf{X}^{(k+1)})^T \mathbf{Y}^{(k)}}{\|\nabla \mathbf{F}(\mathbf{X}^{(k)})\|^2}$$

$$\beta_k = \max \{0, \min\{\beta_k^{\text{FR}}, \beta_k^{\text{PR}}\}\}$$

- (iv) set $\mathbf{p}^{(k+1)} = -\nabla \mathbf{F}(\mathbf{X}^{(k+1)}) + \beta_k \mathbf{p}^{(k)}$;
- (v) set $k = k + 1$;

until a stopping criterion is satisfied.

The implemented stopping criteria are discussed in the following section.

4. Numerical experiments

In this section we present some preliminary numerical results obtained on a digital 3D phantom using Matlab R2018 on a workstation with two Intel processors 230 Ghz equipped with 32 Gb of RAM.

4.1. Experimental setting

We have created a digital version of the *CIRS mod. 015* breast accreditation phantom[‡], used in DBT to quantify the system accuracy. We have used a small version of size $128 \times 128 \times 11$ and we have supposed the phantom constituted of glandular and adipose tissues in different concentrations. In figure 4.1 we show the central slices of the adipose (Figure 2(a)) and glandular (Figure 2(b)) phantom. In an homogeneous background of 50% adipose and 50% glandular tissue, some objects simulate fibers, masses and microcalcifications, that are fundamental features for the early detection of cancers.

Our DBT system has an angular range of $[-17, 17]$ degrees and the tomosynthesis acquisition is performed from 13 equally spaced angles ($N_\theta = 13$); the detector is supposed to have the same area of the xy object plane with $N_p = 128 \times 128$ pixels. The distance between the source and the detector in its central position is 64 cm.

We have considered 37 energy levels ($N_e = 37$) from 10 keV to 28 keV, accordingly to the energy power of a DBT system.

Basing on the concentration values of adipose and glandular tissues in the provided CIRS phantom (as reported in Figure 4.1) a weight reference matrix W_{REF} has been

[‡] This model is described at the url: <http://www.cirsinc.com/products/solution/47/mammographic-accreditation-phantom/>

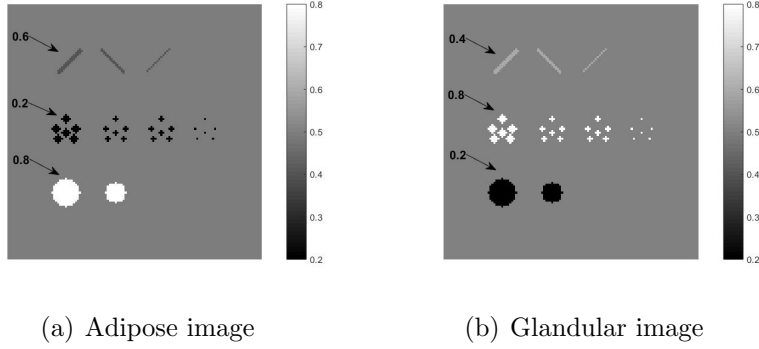


Figure 2. Central slices of the CIRS phantom.

created and the simulated projections have been obtained as:

$$\mathbf{b}_{\text{REF}} = \exp(-\mathbf{A}\mathbf{W}_{\text{REF}}\mathbf{C}^T)\mathbf{s}$$

where \mathbf{A} is the projection matrix computed by a Siddon ray-tracing algorithm [33]. A vector $\boldsymbol{\eta}$ representing white gaussian noise of three different noise levels σ ($\sigma = 10^{-4}$, $\sigma = 5 \cdot 10^{-4}$, $\sigma = 10^{-3}$) is added to \mathbf{b}_{REF} to obtain the data \mathbf{b} :

$$\mathbf{b} = \mathbf{b}_{\text{REF}} + \boldsymbol{\eta}.$$

The image quality is evaluated by means of the Relative Error (RE) between the reference and the computed weight matrices:

$$\text{RE} = \frac{\|\mathbf{W}_{\text{REF}} - \mathbf{W}\|_2}{\|\mathbf{W}_{\text{REF}}\|_2}$$

while the CPU time in seconds is used to measure the computational complexity.

The visual inspection is performed both by showing the resulting images and by plotting profiles along lines in the central layer.

4.2. Numerical results

We present in this section the numerical results obtained on the CIRS digital phantom by using the model (11) with either $\omega(\mathbf{X}) = 0$ and $\omega(\mathbf{X}) = TV_{\beta}(\mathbf{X})$. We compare the NLCG performance with that of the LBFGS method presented in [5] and with the performance of an Accelerated Gradient (AG) method where alternate Barzilai-Borwein rules [27] are employed to accelerate a standard gradient method.

The starting guess $\mathbf{W}^{(0)}$ is, for all the three methods, the constant matrix with values equal to 0.5.

If we consider the methods applied to the non regularized model (1) where $\omega(\mathbf{X}) = 0$, the plot of the RE values vs iterations exhibits semiconvergence, due to the ill-posedness of the problem. In Figure 4.2 we plot the error vs. the iterations (on the left) and the error vs. the computational time in seconds (on the right) for different

noise intensities for the three considered methods. The trend of the curves vs. time is very similar to that vs. iterations, confirming that the iterations of the three methods have approximatively the same computational cost.

As it is well known, the iteration number corresponding to the best relative error decreases when the noise increases. In the case of low noise ($\sigma = 10^{-4}$), 50 iterations are not sufficient to all the three methods to get the best possible result (Figure 3(a)); anyway, we didn't perform more iterations since we are interested in the methods behaviour in the first iterations, in view of a possible application in medical imaging. In that case, the NLCG method is the best performing in time. For a medium noise level $\sigma = 5 \cdot 10^{-4}$, again the NLCG outperforms the others both in terms of precision and speed. Finally, for higher noise $\sigma = 10^{-3}$ all the three methods reach the lowest error in very few iterations and comparable time. In Table 4.3 we report the numerical results in terms of RE values and performed iterations. Since it is practically very difficult to stop the method at its best, we report the results by stopping the method at a fixed early iteration (10 iterations in the case of low and medium noise and 3 iterations in the case of high noise) and we compare it with the best possible result obtained in terms of relative error. We remark that when $\delta = 10^{-4}$ we consider again a maximum of 50 iterations, since the differences between the computed images are not perceivable any more.

Now we analyze the tests performed by using the model (11) with the regularization term $\omega(\mathbf{X}) = TV_\beta(\mathbf{X})$. In this case, all the three methods have been stopped when

$$\frac{\|\mathbf{X}^{(k)} - \mathbf{X}^{(k-1)}\|}{\|\mathbf{X}^{(k-1)}\|} \leq Tol \quad (17)$$

($tol = 10^{-4}$) or after $K_{\max} = 100$ iterations. The reason why we consider a quite large tolerance for the stopping criterium is that the computed images are visually unchanged after that threshold. The regularization parameter γ has been chosen equal to 0.5 by trial and errors as the best compromise for all the considered cases (three methods and three different noise levels).

Figure 4.3 is the counterpart of figure 4.2 for the case of TV_β regularization after 10 iterations of the methods. The AG curve is flat after few iterations and the error almost constant; the LBGFS method decreases but more slowly than NLCG, that outperforms the others for all the noise levels considered, both in terms of efficiency and precision.

Table 4.3 shows the numerical results both after 10 iterations and by stopping the method at convergence, i.e. when (17) is satisfied.

Really, in some of the considered tests, marked by an asterisk, the method stopped because the Armijo backtracking fails after the maximum number of 20 iterations. Hence the computed image is the best reconstruction that can be achieved by the algorithm.

Finally, some images (noise level $\sigma = 5 \cdot 10^{-4}$ on the data) are shown in Figure 4.3 and 4.3 in order to visually evaluate the reconstructions after 10 iterations. In the left column of both figures we report the images obtained by the methods with $\omega(\mathbf{X}) = 0$ and in the right column the images reconstructed by using $\omega(\mathbf{X}) = TV_\beta(\mathbf{X})$.

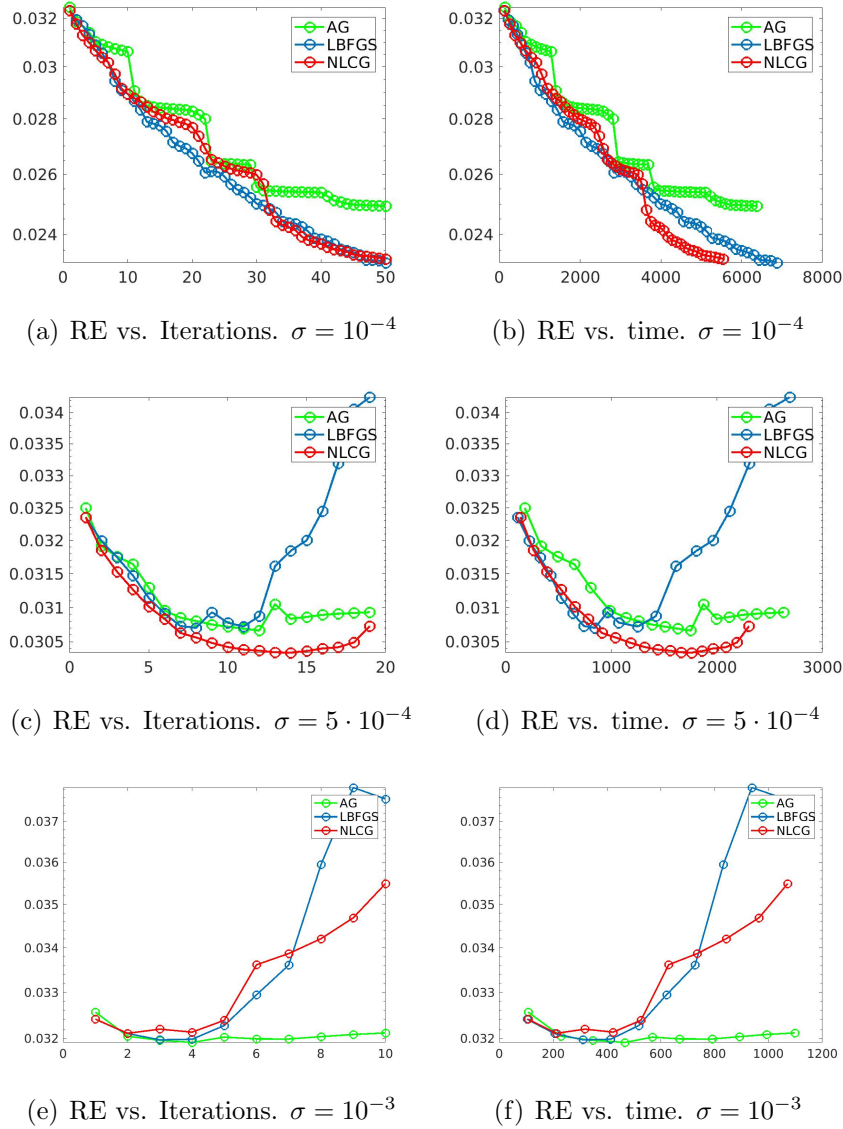


Figure 3. Plot of the RE values vs. iterations (on the left) and vs. computational times in seconds (on the right) for different noise levels σ for the AG (green circles), the LBFGS (blue circles) and the NLCG (red circles) methods in the case $\omega(\mathbf{X}) = 0$.

... qualche commento specifico

4.3. Comments on the results

By comparing the results obtained by the models with $\omega(\mathbf{X}) = 0$ and $\omega(\mathbf{X}) = TV_{\beta}(\mathbf{X})$, the images in Figure ?? and ?? show that the TV regularization improves the quality of the reconstructions by greatly reducing the noise while preserving all the structures, even the smallest micrcalifications constituted by a single pixel. Really, the images appear very sharp after 10 iterations and their enhancement is not significant especially when they are presented in a printable reduced size. Moreover, since fewer iterations are

σ	Method	k max		k optimal	
		RE	k	RE	k
10^{-4}	AG	$3.06 \cdot 10^{-2}$	10	$2.50 \cdot 10^{-2}$	50
	LBFGS	$2.89 \cdot 10^{-2}$	10	$2.31 \cdot 10^{-2}$	50
	NLCG	$2.89 \cdot 10^{-2}$	10	$2.32 \cdot 10^{-2}$	50
$5 \cdot 10^{-4}$	AG	$3.07 \cdot 10^{-2}$	10	$3.06 \cdot 10^{-2}$	12
	LBFGS	$3.07 \cdot 10^{-2}$	10	$3.73 \cdot 10^{-2}$	25
	NLCG	$3.04 \cdot 10^{-2}$	10	$3.03 \cdot 10^{-2}$	14
10^{-3}	AG	$3.20 \cdot 10^{-2}$	3	$3.15 \cdot 10^{-2}$	4
	LBFGS	$3.20 \cdot 10^{-2}$	3	$3.20 \cdot 10^{-2}$	3
	NLCG	$3.22 \cdot 10^{-2}$	3	$3.21 \cdot 10^{-2}$	2

Table 1. Results obtained without regularization ($\omega(\mathbf{X}) = 0$) with AG, LBFGS and NLCG methods at 10 (3 in the case of high noise) fixed iterations (3rd and 4th columns) and at the optimal iteration corresponding to the lowest RE value (5th and 6th columns).

needed to get a similar relative error when $\omega(\mathbf{X}) = TV_{\beta}(\mathbf{X})$ is employed, the TV-based regularization is also computationally convenient (see Figures 4.2 and 4.3).

When the methods are used as iterative regularization methods (case $\omega(\mathbf{X}) = 0$), it is desirable that they have a smooth semiconvergence curve, so that the error doesn't increase too much even if the method is not properly stopped. If we look at Figure 4.2 we observe that LBFGS has a sharp increasing behaviour after semiconvergence. Moreover, it has a higher storage request with respect to the NCLG and AG methods. NLCG gets the best performance for low and medium noise, while the AG method is preferable in the case of high noise.

When the methods are used as solvers of the TV-based regularization problem (case $\omega(\mathbf{X}) = TV_{\beta}(\mathbf{X})$), the NCGL method outperforms the others for all the considered noise levels, since it decreases the relative error very fast in the first iterations. For this reason, it proves to be a very efficient method for this application, where the fast convergence in the first iterations is an essential condition for a practical use in the medical applications.

5. Conclusions

In this paper, a nonlinear conjugate gradient method has been considered for the solution of very large-scale nonlinear least squares problems and, as a case study, the application of such method to DBT imaging has been presented. Regularization by iteration ($\omega(\mathbf{x}) = 0$) and TV-based regularization ($\omega(\mathbf{x}) = TV$) have both been used as stabilizing solution method. The NLCG method has been compared with the AG and LBFGS methods. The numerical results for some test problems based on a digital version of the CIRS Model 015 Mammographic Accreditation Phantom are presented. A visual

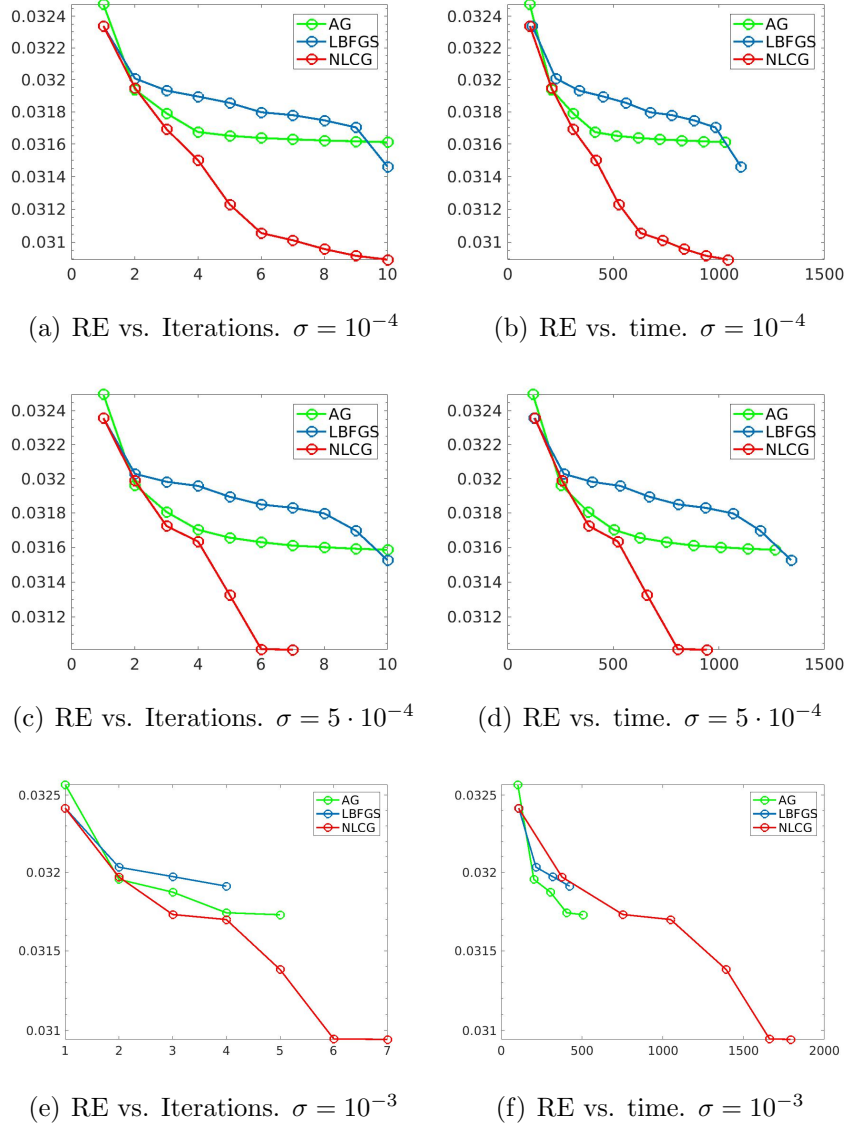


Figure 4. Plot of the RE vs. iterations (on the left) and vs. computational times in seconds (on the right) for different noise levels σ for the AG (green circles), the LBFGS (blue circles) and the NLCG (red circles) methods in the case $\omega(\mathbf{X}) = TV_{\beta}(\mathbf{X})$.

inspection of the restored images suggests that TV-based regularization gives higher visual quality performance than iterative regularization. TV regularization excellently removes the noise but keeps the edges and the small image features. On the other hand, iterative regularization has more noise left on the restorations in order to overcome the image to be blurred. Notice that, iterative regularization has the best quantitative results since TV-based restorations have lower pixel values.

As far as the methods comparison is concerned, the numerical results indicate that the three considered methods have approximately the same computational cost per iteration. Moreover, they suggest that the NLCG method tends to combine the positive features of both LBFGS and AG methods. In fact, it exhibits fast convergence

σ	Method	k max		k conv.	
		RE	k	RE	k
10^{-4}	AG	$3.16 \cdot 10^{-2}$	10	$3.16 \cdot 10^{-2}$	8
	LBFGS	$3.14 \cdot 10^{-2}$	10	$3.13 \cdot 10^{-2}$	12
	NLCG	$3.10 \cdot 10^{-2}$	10	$3.08 \cdot 10^{-2}$	14
$5 \cdot 10^{-4}$	AG	$3.16 \cdot 10^{-2}$	10	$3.16 \cdot 10^{-2}$	9
	LBFGS	$3.15 \cdot 10^{-2}$	7*	$3.07 \cdot 10^{-2}$	19
	NLCG	$3.09 \cdot 10^{-2}$	7*	$3.10 \cdot 10^{-2}$	7*
10^{-3}	AG	$3.17 \cdot 10^{-2}$	10	$3.17 \cdot 10^{-2}$	6
	LBFGS	$3.14 \cdot 10^{-2}$	10	$2.80 \cdot 10^{-2}$	49
	NLCG	$3.09 \cdot 10^{-2}$	7*	$3.09 \cdot 10^{-2}$	7*

Table 2. Results obtained with TV regularization ($\omega(\mathbf{X}) = TV_{\beta}(\mathbf{X})$) with AG, LBFGS and NLCG methods at 10 fixed iterations (3rd and 4th columns) and at the iteration satisfying the stopping criterium (17) (5th and 6th columns). The asterisk indicates failure in the linesearch procedure.

as the LBFGS method, by quickly reducing the relative errors values in the very first iterations and, as the AG method, it does not require the solution of an ill-conditioned linear system.

The promising numerical results stimulate future deeper analyses of the behavior of nonlinear conjugate gradient methods for the solution of large-scale nonlinear inverse problems.

Acknowledgements

This research has been partially supported by GNCS-INDAM Italy.

References

- [1] et al K K 1992 *Comp. med. Imag. Graph.* **89** 5675–5679
- [2] et al D M 2013 *Nature* **495** 187–192
- [3] Elbakri I A and Fessler J A 2002 *IEEE Trans. Med. Imaging* **21** 89–99
- [4] Duan J, Li S, Hu W and Su J 1999 *Comp. Med. Im. Graph.* **23** 173–179
- [5] landi G, Piccolomini E L and Nagy J 2017 *Inv. Probl.* **33** 95005
- [6] Bustamante V, Nagy J, Feng S and Sechopoulos I 2013 *SIAM J. Scient. Comput.* **135** S192–S208
- [7] Engl H W, Hanke M and Neubauer A 2000 *Regularization of Inverse Problems* (Dordrecht: Kluwer Academic Publishers)
- [8] Hansen P C 2010 *Discrete Inverse Problems: Insight and Algorithms* (Philadelphia, PA: SIAM)
- [9] Mueller J L and Siltanen S 2012 *Linear and Nonlinear Inverse Problems with Practical Applications* (Philadelphia, PA: SIAM)
- [10] Vogel C R 2002 *Computational Methods for Inverse Problems* (Philadelphia, PA: SIAM)

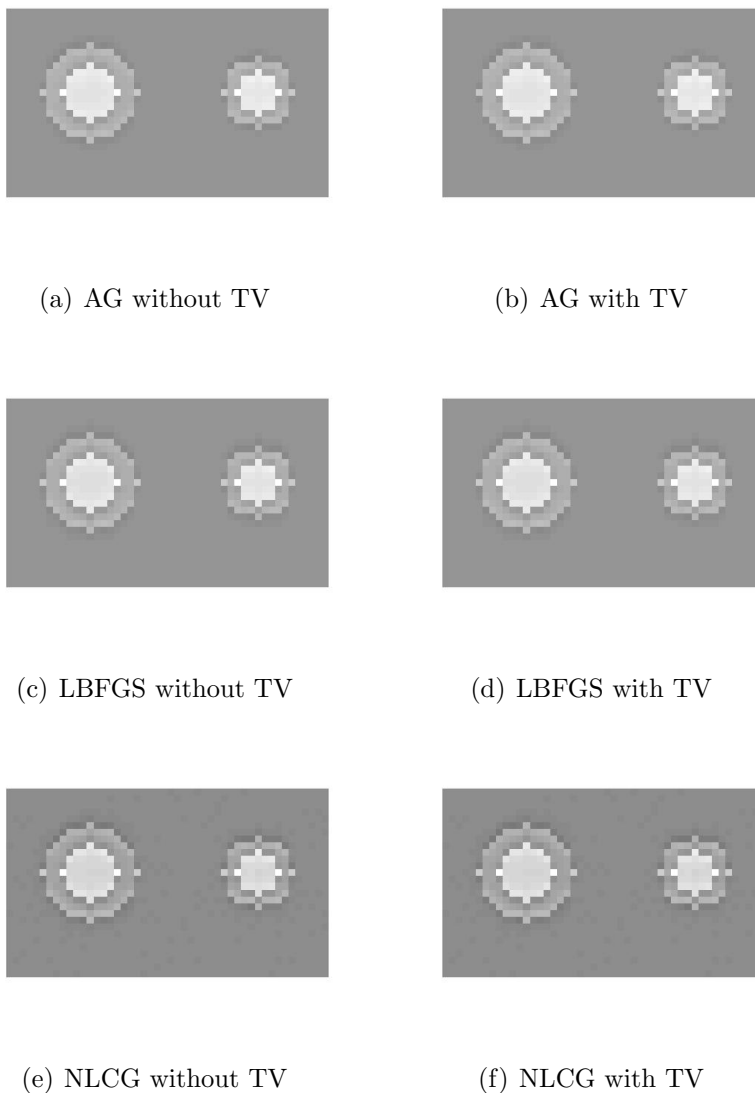


Figure 5. Microcalcifications in the adipose central layer reconstructed by AG, LBFGS and NLCG methods in the case $\sigma = 5 \cdot 10^{-4}$ after 10 iterations of the methods.

- [11] Zhang J, Hu Y and G Nagy J 2018 *Comput. Med. Imaging Graph.* **12** 239–259 URL <http://aims sciences.org//article/doi/10.3934/ipi.2018010>
- [12] Hager W and Zhang H 2006 *Pacific journal of Optimization* **2** 35–58
- [13] Touati-Ahmed D and Storey C 1990 *J. Optim. Theory Appl.* **64** 379–397
- [14] Gobbins J and Godfrey D 2003 *Phys. Med. Biol.* **48** R65–R106
- [15] JM P and et al F E J 2007 *Radiographics* **27** S231–40
- [16] Males M, Mileta D and Grgic M 2011 Digital Breast Tomosynthesis: a technological reviews *53th International Symposium ELMAR* pp 41–45
- [17] Sidky E Y, Pan X, Reiser I S and Nishikawa R M 2009 *Med. Phys.* **36** 4920–4932
- [18] Yu H and Wang G 2010 *Phys. Med. Biol.* **55** 3905–3916
- [19] Piccolomini E L and Morotti E 2016 *J. Algor. and Computat. Techn.* **10** 277–289
- [20] adn G Di Chiro R A B 1976 *Phys. Med. Biol.* **2** 390–398
- [21] Foygel Barber R, Sidky E Y, Gilat Schmidt T and Pan X 2016 *Phys. Med. Biol.* **61** 3784–3818

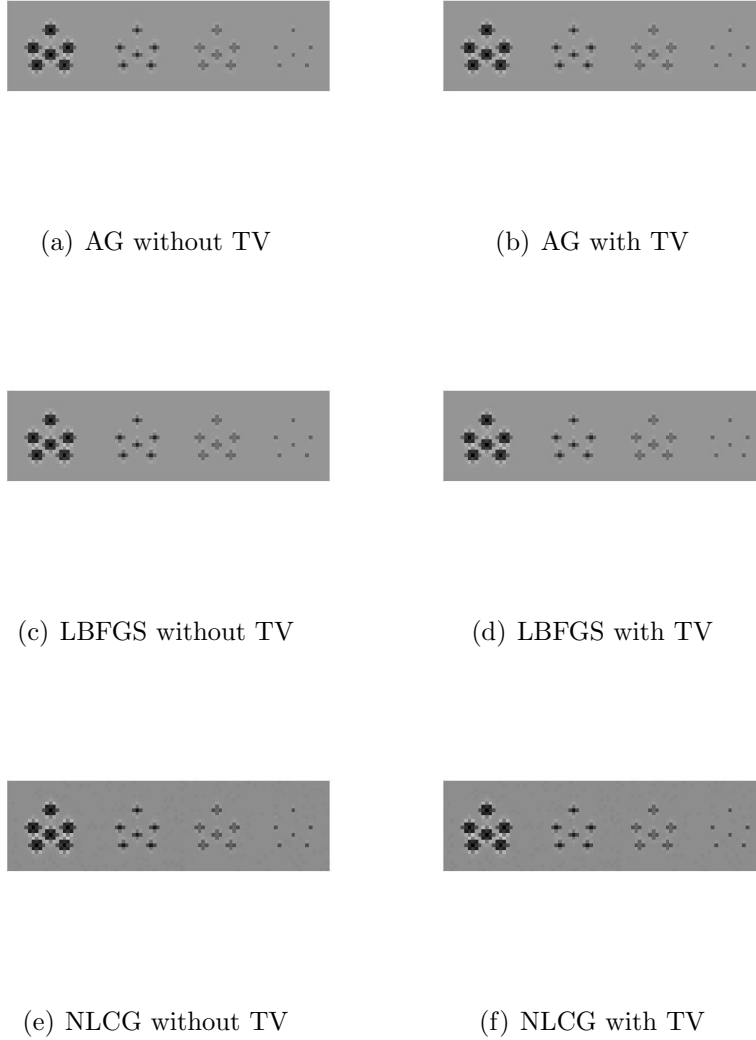


Figure 6. Masses in the adipose central layer reconstructed by AG, LBFGS and NLCG methods in the case $\sigma = 5 \cdot 10^{-4}$ after 10 iterations of the methods.

- [22] O’Sullivan J A and Benac J 2007 *IEEE Trans. Med. Imaging* **26** 283–297
- [23] Alvarez R E, Seibert J A and Thompson S K 2004 *Med. Phys.* **31** 556–565
- [24] Heismann B and Balda M 2009 *Med. Phys.* **36** 4471–4485
- [25] Epstein C L 2007 *Introduction to the Mathematics of Medical Imaging, Second Edition* 2nd ed (SIAM, Philadelphia)
- [26] Barzilai J and Borwein J 1988 *IMA J. Numer. Anal.* **8** 141–148
- [27] Bonettini S, Zanella R and Zanni L 2009 *Inv. Probl.* **25**
- [28] Piccolomini E L, Coli V L, Morotti E and Zanni L 2018 *Comput. Optim. Appl.* **71** 171191
- [29] Landi G, Piccolomini E L and Nagy J G 2015 *Journal of Physics: Conference Series* **657** 012006
- [30] Erway J and Marcia R F 2012 *Linear Algebra Appl.* **437** 333–344
- [31] Fletcher R and Reeves C M 1964 *Computer Journal* **7** 149–154
- [32] Polak E and Ribiere G 1969 *R.I.R.O.* **16** 35–43
- [33] Siddon R L 1985 *Med. Phys.* **12** 252–255